Mapping sub-surface structure of thin films in three dimensions with an optical near-field

Oliver Fenwick, Soumaya Mauthoor and Franco Cacialli.**

Dr. O. Fenwick
School of Engineering and Materials Science, Queen Mary University of London, London WC1E 6BT, United Kingdom.
Email: o.fenwick@qmul.ac.uk

Dr. S. Mauthoor and Prof. F. Cacialli
Department of Physics and Astronomy and London Centre for Nanotechnology, University College London, Gower Street, London WC1E 6BT, United Kingdom.
Email: f.cacialli@ucl.ac.uk

Subsurface mapping is crucial to understanding many biological systems as well as structured thin films for (opto)electronic or photonic applications. A non-invasive method is presented to map subsurface nanostructures from scanning near-field optical microscopy images. The Bethe-Bouwkamp model is used to simulate imaging of buried nano objects or subsurface slanted planar interfaces, and it is shown how to determine their depth and size, or the interface inclination, from just one image. It is shown that the steep optical field gradient makes near-field microscopy a particularly sensitive depth probe for thin films.

1. Introduction

In all fields of knowledge the ability to see through and beyond surfaces is intimately connected with deeper understanding of phenomena. Within natural sciences, sub-surface imaging is crucial to the study of a large variety of "natural" nanostructures (from sub-cellular elements in living organisms to mixed phases and defects in a variety of materials) as well as of artificial, man-made systems, that can be generated via either lithographic methods[1] or via entropy-driven phase-separation processes, [2] including the growth of quantum dots[3] for single-photon sources, or in the study of defects in electronic devices.[4] Successful implementation of nanotechnology requires a variety of high-resolution microscopy techniques,[5] for both surfaces and the bulk, and this demand has been met with remarkable advances in far-field nanoscale resolution optical microscopy, some of which were rewarded with the 2014 Nobel prize in chemistry. There is also vast interest in the optical near-field for probing surface structure in non-biological domains since it does not rely on dyes with specific photoluminescence properties and can also be applied beyond fluorescence imaging. Detecting the optical near-field typically requires a probe to be positioned at nanometre distances from the surface under study, but with the development of the far-field superlens method for viewing the evanescent optical near-field at far-field distances,[6] imaging of such evanescent optical fields has become a practical technique for obtaining structural information of samples across an increasingly broad cross-section of science and engineering.

Scanning near-field optical microscopy (SNOM) has proved to be a powerful tool to achieve sub-wavelength resolution in both imaging[7] and fabrication[7a, 8] of a variety of nanostructures, in particular for its capabilities in obtaining simultaneous topographical and photoluminescence images[7b, 9] - and often further information such as the local photoconductivity,[10] polarisation,[1a, 11] surface plasmons,[12] mechanical stress,[13] Raman signal,[13b, 14] thickness,[15] dichroism[16] or the chemical composition[17] of the sample. As with other members of the scanning probe family of techniques, SNOM is primarily aimed at surface characterisation, although the nature of the evanescent optical field allows a degree of

sub-surface probing. A small number of studies have accordingly reported detection of nanoscale subsurface optical structure with SNOM,[6, 18] or by using other techniques such as cathodoluminescence spectroscopy[5b] and scanning superlens microscopy.[5c] Importantly, the steep decay of the optical field from the SNOM probe makes it sensitive to the depth of objects in films, and therefore information about the location of objects in three dimensions (3D) could be obtained in a unique way that is both highly sensitive and non-destructive – not unlike scanning acoustic holography,[19] but with optical contrast.

By definition, near-field imaging occurs when the sub-wavelength probe and the sample are located less than the order of a wavelength apart, and accordingly a range of apertured[20] and apertureless[21] probes have been developed to guide laser light near the sample. The probe tip can be used as a nanosource for illuminating a sample or conversely for collecting the evanescent field from it. The results we present simulate illumination-mode apertured photoluminescence (PL) and photocurrent (PC) SNOM, which is quite different from scattering SNOM (s-SNOM), for which a method has been proposed to extract 3D structure either from multiple images obtained in volume scanning mode,[22] or through phase-sensitive detection.[16] Neither multiple images nor phase- sensitive detection are required in the method we present – indeed phase is not preserved in either PL or PC SNOM. Our samples are topographically smooth, but optically inhomogeneous, and the imaging is simulated using a model of the near-field pioneered by Bethe[23] that considers transmission of light through a sub-wavelength circular aperture in an perfectly conducting metal sheet. It is regularly used in near-field investigations[24] because of its parallels with the geometry of an apertured probe and, despite its approximations,[25] encapsulates the physics of the near-field problem.

2. Methods

We consider the sample to have a linear response to illumination, introducing a parameter $\eta(\boldsymbol{R})$ relating to the sample's optical properties such as PL or PC efficiency at a position $\boldsymbol{R} = (\boldsymbol{r}, z) = (x, y, z)$ within the sample. The plane $z = 0$ is defined as being the surface of the (planar) sample (which is parallel to the aperture plane). The total collected signal $I(\boldsymbol{\Gamma})$ when the SNOM probe is centred at a lateral position $\boldsymbol{\Gamma} = (x', y')$ is therefore the sum of the product of the intensity, $F(\boldsymbol{R})$, of the optical field with the material response, $\eta(\boldsymbol{R})$, over a volume defined by the thickness of the sample and lateral extent of the near-field.

$$I(\boldsymbol{\Gamma}) = \sum_{\boldsymbol{R}} F(\boldsymbol{R}, \boldsymbol{\Gamma})\eta(\boldsymbol{R}) \tag{1}$$

$F(\boldsymbol{R},\boldsymbol{\Gamma})$ is calculated by the downwards propagation of the x- and y-polarised components of the optical field that exists inside the film at the top surface, $E_s(\boldsymbol{k})$.

$$F(\boldsymbol{R}, \boldsymbol{\Gamma}) = \left(\iint [E_s(\boldsymbol{k})]_x \exp i(\boldsymbol{k}.(\boldsymbol{r} - \boldsymbol{\Gamma}) + z\kappa_s)\, d\boldsymbol{k}\right)^2 + \left(\iint [E_s(\boldsymbol{k})]_y \exp i(\boldsymbol{k}.(\boldsymbol{r} - \boldsymbol{\Gamma}) + z\kappa_s)\, d\boldsymbol{k}\right)^2 \tag{2}$$

$k = (k_x, k_y)$ is the wavevector in the x-y plane, and κ_s is the wavenumber in the z-direction.

$$\kappa_s = \sqrt{{n_{film}}^2 {k_0}^2 - k^2} \tag{3}$$

where n_{film} is the refractive index of the film and $k_0 = 2\pi/\lambda$ is the wavenumber in air. $E_s(k)$ derives from the application of electromagnetic boundary conditions to the Bethe-Bouwkamp near-field computed on the air side of the interface and the resultant components of $E_s(k)$ are linear combinations of the orthogonally polarised components on the air side. Note that although light incident on the SNOM aperture is linearly polarised, the near-field contains two orthogonally polarised components as a result of the aperture diffraction. The form of $E_s(k)$ is described in detail elsewhere.[24b] Our samples are flat with a complex refractive index of the sample, n, of $1.62+0.54i$, corresponding to that of

poly(p-phenylene vinylene), PPV, at 325 nm, as measured by spectroscopic ellipsometry.[9c] An aperture radius, a, of 20 nm is used, with the tip-sample distance, z_0, set to 5 nm.

3. Results and discussion

We first studied the signal generated when a probe crosses over a non-luminescent spherical object (η = 0) embedded in a 100 nm thick luminescent matrix (η = 1) (Figure 1b) and sought to quantify relevant parameters of the embedded spheres by firstly exploiting the full-width at half-maximum (FWHM) of their intensity in the linescans. Figure 1c shows these FWHM of linescans across a 22 nm diameter sphere as a function of its depth in the film (as measured from the position of its centre), with the incident laser polarisation both parallel (full circles) and perpendicular (empty circles) to the scan direction. Plotted as continuous and dashed lines is the FWHM of the near-field profile in a uniform sample in the directions parallel and perpendicular respectively to the incident laser polarisation. The sphere is comparable in size to the diameter of the aperture (40 nm) and is larger than the decay length of the optical field, with the bottom of the sphere being imaged by a field which is approximately twice as broad and, in some cases, more than an order of magnitude lower in intensity compared to the field at the sphere's top. In spite of such a steep optical field gradient, which decays and diverges over a distance comparable to the diameter of the object, the size of the object in the image correlates strongly with the width of the optical field at the depth of the centre of the sphere - a regime which holds for objects up to 50 nm in diameter. Such a close correlation across a range of object sizes (including some larger than the aperture diameter) is surprising, and as a consequence of this observation it is relatively straightforward to extract object depths from such an image.

This is confirmed in Figure 2b, showing the FWHM of linescans across spheres embedded at two different depths (24 nm and 48 nm), as a function of the sphere radius. The FWHM of the line-scan is almost independent of the sphere diameter when less than 50 nm, and only changes by 2 nm or less as it is increased to 70 nm. Importantly, this means that the apparent size of such sub-wavelength objects in the image can be used as a reliable measure of their depth with nanometre precision. Therefore, the computational time to extract information about sub-surface object depths can be much reduced, since only simulation of the FWHM of the near-field as a function of depth is required, rather than a full 3D simulation of the sample geometry. Furthermore, rotating the incident laser polarisation direction gives us two independent ways of extracting this information.

Once the depth of the sphere is known, its radius can be extracted using the dip of intensity in the image, I_{dip} (Figure 1b), and comparing with simulated data such as that shown in Figure 2c. Unlike the apparent width of objects, I_{dip} is highly dependent on their size, changing over four orders of magnitude when the diameter is varied over just one order (for spheres embedded at 48nm). This makes I_{dip} a highly sensitive measure of the size of nanoscale objects, with the ultimate limitation being the detection sensitivity of the microscope.

We then investigated a different sample geometry, simulating the signal intensity as the apertured probe crosses a slanted planar interface, inclined at angle θ, between two regions with different PL or PC efficiencies, η. This situation occurs for example between n and p-doped regions of a semiconductor. Saiki et al. [26] have reported a method using multiwavelength photocurrent SNOM to determine the inclination of a slanted 1 μm thick p-n junction which intersects the sample surface. This method, though successful, exploits propagating modes in the sample (from a 200 nm aperture) at significantly lower resolution and is less applicable to thin film devices where the near-field dominates the imaging. Other far-field techniques such as confocal microscopy have a depth of field much larger than the thickness of thin films (~100 nm), making them unsuitable for extracting structural information from partially submerged heterojunctions.

For simplicity we set $\eta = 0$ on one side of the interface and $\eta = 1$ on the other. A schematic of the sample profile for a 60 nm deep film is shown in Figure 3a, with corresponding simulated image linesections in Figure 3b for different inclinations. As expected, the signal intensity rises smoothly across the interface, and levels out at large distances from it. For steep interfaces ($\theta < 15^o$) the linescans are almost indistinguishable, and the position where the interface intersects the surface coincides with the position where the signal intensity rises to half its maximum. For shallow interfaces ($\theta > 15^o$) the linescans become rapidly asymmetric and the signal changes more gradually, as one might expect since shallower interfaces have a greater lateral extent. This invites the possibility of distinguishing between experimentally investigated interfaces. The first derivative of the signal intensity, and in particular its FWHM (χ in Figure 3c), permits us to do this in a quantitative fashion. Figure 3c plots the first derivative of the linescans, and shows a broadening and flattening as the inclination angle increases, whilst its position moves away from where the interface meets the surface. This is shown more quantitatively in Figure 4a, where the FWHM of the first derivative is plotted against the tangent of the interface inclination angle. For large angles ($\theta > 45^o$) the FWHM has a strongly linear relationship to the tangent of the inclination angle, since the lateral width of the interface scales as $tan(\theta)$. The asymmetry relative to the incident laser polarisation once again provides two independent ways of extracting the inclination angle.

We can, in principle, discriminate between inclination angles with $\theta<15^0$ by using the second derivative of the linescans. Figure 3d shows the second derivative of the four linescans across the slanted heterojunctions shown in Figure 3b. It can be seen that the position of the inflection point (second derivative = 0) has a dependence on the angle of inclination. The separation between the inflection point, and the maximum and minimum of the second derivative - Δ_{max} and Δ_{min} respectively - are plotted in Figure 4b. When the interface is perpendicular to the polarisation direction, Δ_{max} and Δ_{min} change by >50% when the angle of inclination is increased from 0° to 76°; and they still change by >10% when the interface angle is increased from 0° to 15°. This allows for the identification of its inclination even at low θ, though experimentally this latter method would be challenging since small levels of noise may become quite significant when plotting the second derivative.

4. Conclusions

The SNOM is designed and used predominantly for mapping a number of surface properties of materials. We have presented simulations which give precious insight into how the SNOM could also be used as a powerful non-destructive tomographic tool for probing thin films in their sub-surface regions. We have shown that a single image can be enough to accurately determine both the depth and size of sub-wavelength sized inclusions in thin films. Similarly, the sub-surface properties of domain boundaries can be investigated in a quantitative manner using the SNOM, in particular to extract the angle of a sub-surface planar interface with respect to the surface. We do, however, note some limitations to this technique such as the difficulty in accurately determining the slope of steep interfaces.

Our work highlights a simple approach that can be applied across a range of SNOM modes and experiments, but different experiments to the one presented here would inevitably involve different optical properties and geometries of the system, including aperture size, sample refractive index and laser wavelength. The laser wavelength is generally selected to match the optical properties of the sample in order to balance optical response with sufficient depth penetration of the optical field, in order that the subsurface structure can be studied. No material has a perfectly sharp absorption edge, but rather, absorption edges are usually distributed over several tens of nanometres of spectral width, thereby making it entirely feasible to reduce absorption via wavelength tuning of the beam used for the SNOM investigation. Beyond absorption by the sample, the penetration depth of the nearfield into the film is determined by the nearfield attenuation length, $|\boldsymbol{\kappa_s}|^{-1}$. For a given aperture diameter, equation (3) above implies that longer laser wavelengths have a greater nearfield character and consequently experience a higher attenuation rate (in the z direction) of high spatial resolution components of the

optical field (in the *x, y* directions), thereby effectively allowing the user to balance imaging resolution and overall penetration depth into the sample. The sample refractive index also has a strong effect both on the transmission of light across the air-sample interface (due to reflection of certain wavevectors at the air-sample interface), and also on the attenuation length, $|\boldsymbol{\kappa}_s|^{-1}$, of the nearfield within the sample (Eqs. (2) and (3)).[24b] Quantitative analysis of any future experiment should therefore involve adaptation of our method by re-calculation of the nearfield distribution using the optical parameters of the experiment being simulated.

Finally, we note that it is the evanescent nature of the optical excitation from the SNOM which makes it particularly sensitive to the position and geometry of sub-surface features – much more so than conventional far-field optical microscopies.

Acknowledgements

We thank the EPSRC and the EC for financial support received within the context of the following grants/projects: EU-contracts MRTN-CT-2006-036040 – THREADMILL; PITN-GA-2009–238177 – SUPERIOR; PIEF-GA-2012-326666 – MULTITUDES; grant agreement N. 212311 - ONE-P project (FP7 2007-2013); and the EPSRC/NanoSci-Era+project SENSORS. We also thank LOT Oriel for measuring the complex refractive index of PPV films. OF would like to acknowledge the Royal Society for his University Research Fellowship (UF140372). FC is a Royal Society Wolfson Foundation Research Merit Award holder.

References

[1] a) E. Betzig, J. K. Trautman, J. S. Weiner, T. D. Harris, R. Wolfe, *Appl. Opt.* **1992**, *31*, 4563; b) O. Fenwick, L. Bozec, D. Credgington, A. Hammiche, G. M. Lazzerini, Y. R. Silberberg, F. Cacialli, *Nat. Nanotechnol.* **2009**, *4*, 664; c) R. F. Service, *Science* **2001**, *293*, 785.

[2] S. Brovelli, F. Meinardi, G. Winroth, O. Fenwick, G. Sforazzini, M. J. Frampton, L. Zalewski, J. A. Levitt, F. Marinello, P. Schiavuta, K. Suhling, H. L. Anderson, F. Cacialli, *Adv. Funct. Mater.* **2010**, *20*, 272.

[3] A. F. Jarjour, R. A. Taylor, R. A. Oliver, M. J. Kappers, C. J. Humphreys, A. Tahraoui, *Appl. Phys. Lett.* **2008**, *93*, 233103.

[4] M. H. Gray, J. W. P. Hsu, L. Giovane, M. T. Bulsara, *Phys. Rev. Lett.* **2001**, *86*, 3598.

[5] a) P. A. Midgley, R. E. Dunin-Borkowski, *Nat. Mater.* **2009**, *8*, 271; b) A. C. Atre, B. J. M. Brenny, T. Coenen, A. García-Etxarri, A. Polman, J. A. Dionne, *Nat. Nanotechnol.* **2015**, *10*, 429; c) F. Wang, L. Liu, H. Yu, Y. Wen, P. Yu, Z. Liu, Y. Wang, W. J. Li, *Nat. Commun.* **2016**, *7*, 13748.

[6] Z. Wang, W. Guo, L. Li, B. Luk'yanchuk, A. Khan, Z. Liu, Z. Chen, M. Hong, *Nat. Commun.* **2011**, *2*, 218.

[7] a) E. Betzig, J. K. Trautman, *Science* **1992**, *257*, 189; b) J. Chappell, D. G. Lidzey, P. C. Jukes, A. M. Higgins, R. L. Thompson, S. O'Connor, I. Grizzi, R. Fletcher, J. O'Brien, M. Geoghegan, R. A. L. Jones, *Nat. Mater.* **2003**, *2*, 616.

[8] a) D. V. Cotton, C. J. Fell, W. J. Belcher, P. C. Dastoor, *J. Phys. D: Appl. Phys.* **2008**, *41*, 195107; b) D. Credgington, O. Fenwick, A. Charas, J. Morgado, K. Suhling, F. Cacialli, *Adv. Funct. Mater.* **2010**, *20*, 2842.

[9] a) A. Harootunian, E. Betzig, M. Isaacson, A. Lewis, *Appl. Phys. Lett.* **1986**, *49*, 674; b) O. Fenwick, G. Latini, F. Cacialli, *Synt. Met.* **2004**, *147*, 171; c) B. Hecht, H. Bielefeldt, Y. Inouye, D. W. Pohl, L. Novotny, *J. Appl. Phys.* **1997**, *81*, 2492; d) S. Brovelli, H. Guan, G. Winroth, O. Fenwick, F. Di Stasio, R. Daik, W. J. Feast, F. Meinardi, F. Cacialli, *Appl. Phys. Lett.* **2010**, *96*; e) R. Stevenson, R. Riehn, R. G. Milner, D. Richards, E. Moons, D. J. Kang, M. Blamire, J. Morgado, F. Cacialli, *Appl. Phys. Lett.* **2001**, *79*, 1921.

[10] a) C. R. McNeill, H. Frohne, J. L. Holdsworth, J. E. Furst, B. V. King, P. C. Dastoor, *Nano Lett.* **2004**, *4*, 219; b) R. Riehn, R. Stevenson, D. Richards, D. J. Kang, M. Blamire, A. Downes, F. Cacialli, *Adv. Funct. Mater.* **2006**, *16*, 469.

[11] a) H. Fischer, A. Nesci, G. Leveque, O. J. F. Martin, *J. Microsc. Oxford* **2008**, *230*, 27; b) A. E. Klein, N. Janunts, M. Steinert, A. Tunnermann, T. Pertsch, *Nano Lett.* **2014**, *14*, 5010.

[12] a) J. N. Chen, M. L. Nesterov, A. Y. Nikitin, S. Thongrattanasiri, P. Alonso-Gonzalez, T. M. Slipchenko, F. Speck, M. Ostler, T. Seyller, I. Crassee, F. H. L. Koppens, L. Martin-Moreno, F. J. G. de Abajo, A. B. Kuzmenko, R. Hillenbrand, *Nano Lett.* **2013**, *13*, 6210; b) A. V. Zayats, I. I. Smolyaninov, A. A. Maradudin, *Phys. Rep.* **2005**, *408*, 131.

[13] a) A. M. Gigler, A. J. Huber, M. Bauer, A. Ziegler, R. Hillenbrand, R. W. Stark, *Opt. Express* **2009**, *17*, 22351; b) S. Webster, D. N. Batchelder, D. A. Smith, *Appl. Phys. Lett.* **1998**, *72*, 1478.

[14] a) M. Namboodiri, T. Z. Khan, S. Bom, G. Flachenecker, A. Materny, *Opt. Express* **2013**, *21*, 918; b) P. G. Gucciardi, S. Trusso, C. Vasi, S. Patanè, M. Allegrini, *Appl. Opt.* **2003**, *42*, 2724.

[15] a) Z. Liu, Y. Zhang, S. W. Kok, B. P. Ng, Y. C. Soh, *Opt. Express* **2010**, *18*, 3298; b) P. Karageorgiev, H. Orendi, B. Stiller, L. Brehmer, *Appl. Phys. Lett.* **2001**, *79*, 1730.

[16] F. Tantussi, F. Fuso, M. Allegrini, N. Micali, I. G. Occhiuto, L. M. Scolaro, S. Patane, *Nanoscale* **2014**, *6*, 10874.

[17] a) D. A. Kossakovski, S. D. O'Connor, M. Widmer, J. D. Baldeschwieler, J. L. Beauchamp, *Ultramicroscopy* **1998**, *71*, 111; b) A. J. Huber, J. Wittborn, R. Hillenbrand, *Nanotechnology* **2010**, *21*, 235702.

[18] a) I. T. Lucas, A. S. McLeod, J. S. Syzdek, D. S. Middlemiss, C. P. Grey, D. N. Basov, R. Kostecki, *Nano Lett.* **2015**, *15*, 1; b) T. Taubner, F. Keilmann, R. Hillenbrand, *Opt. Express* **2005**, *13*, 8893; c) S.

Dai, M. Tymchenko, Z.-Q. Xu, T. T. Tran, Y. Yang, Q. Ma, K. Watanabe, T. Taniguchi, P. Jarillo-Herrero, I. Aharonovich, D. N. Basov, T. H. Tao, A. Alù, *Nano Lett.* **2018**, *18*, 5205; d) A. A. Govyadinov, S. Mastel, F. Golmar, A. Chuvilin, P. S. Carney, R. Hillenbrand, *ACS Nano* **2014**, *8*, 6911.

[19] G. S. Shekhawat, V. P. Dravid, *Science* **2005**, *310*, 89.

[20] S. Munster, S. Werner, C. Mihalcea, W. Scholz, E. Oesterschulze, *J. Microsc. Oxford* **1997**, *186*, 17.

[21] F. Zenhausern, M. P. Oboyle, H. K. Wickramasinghe, *Appl. Phys. Lett.* **1994**, *65*, 1623.

[22] Z. B. Wang, W. Guo, L. Li, B. Luk'yanchuk, A. Khan, Z. Liu, Z. C. Chen, M. H. Hong, *Nat. Commun.* **2011**, *2*.

[23] H. A. Bethe, *Phys. Rev.* **1944**, *66*, 163.

[24] a) R. Riehn, A. Charas, J. Morgado, F. Cacialli, *Appl. Phys. Lett.* **2003**, *82*, 526; b) R. Stevenson, D. Richards, *Semicond. Sci. Technol.* **1998**, *13*, 882; c) D. Vanlabeke, D. Barchiesi, F. Baida, *J. Opt. Soc. Am. A* **1995**, *12*, 695.

[25] a) A. Drezet, S. Huant, J. C. Woehl, *J. Lumin.* **2004**, *107*, 176; b) K. Tanaka, M. Tanaka, *Appl. Opt.* **2004**, *43*, 1734.

[26] T. Saiki, N. Saito, J. Kusano, M. Ohtsu, *Appl. Phys. Lett.* **1996**, *69*, 644.

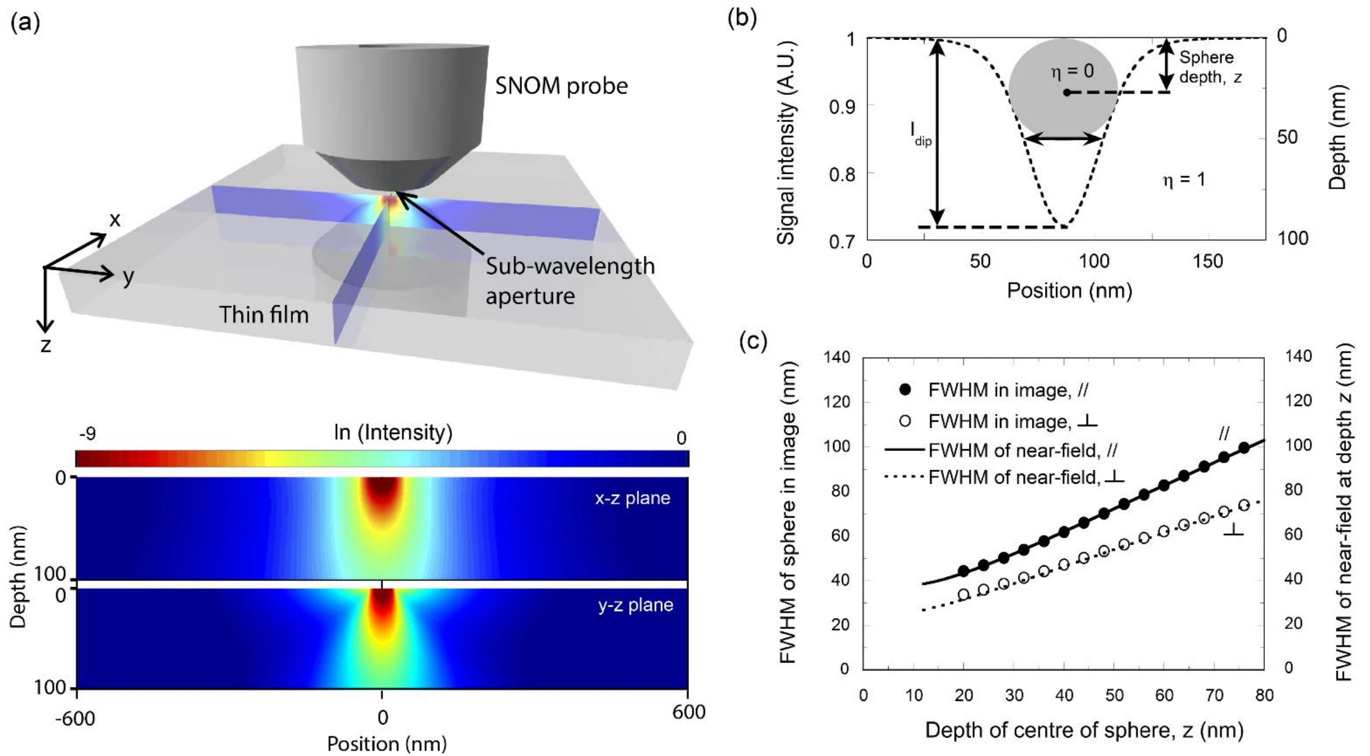

Figure 1. **a** Schematic of the probe-sample geometry. The example field shown in x-z and y-z cross-sections is calculated for an aperture of radius 20 nm positioned 5 nm above a 100 nm thick PPV sample and illuminated normally by a 325 nm laser polarized in the x-direction. **b** Schematic of a 48 nm diameter sphere with a PL or PC efficiency of zero, embedded at 24 nm in a 100 nm deep matrix with a PC or PL efficiency of unity. Superimposed (dashed line) is the signal intensity as the aperture crosses the sphere. **c** Width (full-width at half-maximum, FWHM) of signal intensity, I_{dip}, when scanning across a 22 nm diameter sphere (circles), as a function of its depth (measured from its centre to the film surface). The continuous lines report the FWHM of the intensity profile of the near-field (lines) in a uniform film (no sphere) as a function of depth (distance from the surface). Results with the incident laser polarisation direction both parallel (solid) and perpendicular (empty/dashed) to the scanning direction are plotted. A remarkable correlation can be seen between the FWHM of the near-field at a certain depth and the FWHM in the image of the sphere centred at that depth.

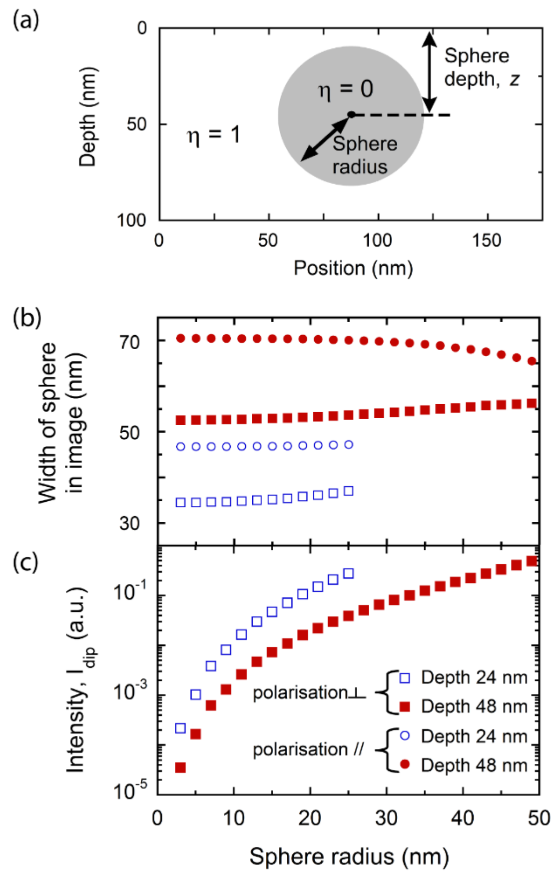

Figure 2 (a) A schematic of the buried nano-object model, comprising of a spherical inclusion in a thin film. (b) Full width at half maximum (FWHM) of sphere as it appears in the image, and (c) Maximum change in signal intensity, I_{dip}, of linescans across spheres embedded at two different depths, as a function of the sphere radius. Widths in the image are shown both with the incident light polarisation direction perpendicular (empty) and parallel (full) to the scanning direction. Data are truncated to included only for sphere radii that do not intersect the boundaries of the film. It should also be noted that for a spherically symmetric object, I_{dip} is independent of the polarisation direction, so data for just one polarisation is displayed in b.

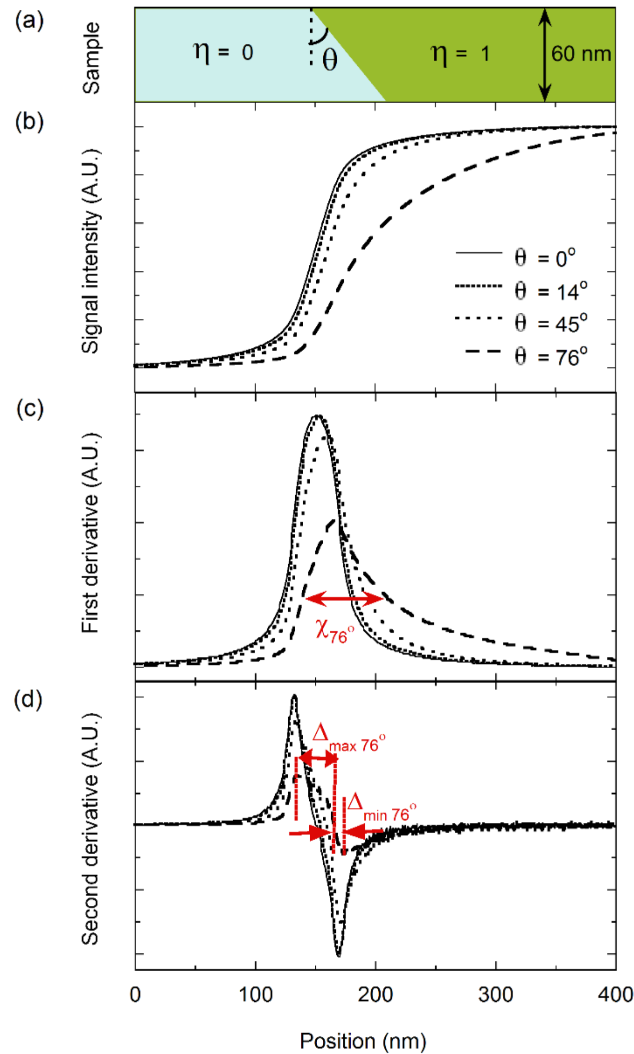

Figure 3 a Schematic of the slanted heterojunction simulated sample. B Signal intensity of a linescan perpendicular to the heterojunction. c FWHM of the first derivative of the signal across a slanted heterojunction, with the incident laser polarisation direction parallel (circles) and perpendicular (squares) to the interface, plotted against the tangent of the inclination angle. d Separation between the point of inflexion of the signal intensity across a slanted heterojunction, and both the maximum (filled symbols) and the minimum (empty symbols) of its second derivative. Results both with the incident light polarisation direction parallel (circles) and perpendicular (squares) to the interface are plotted.

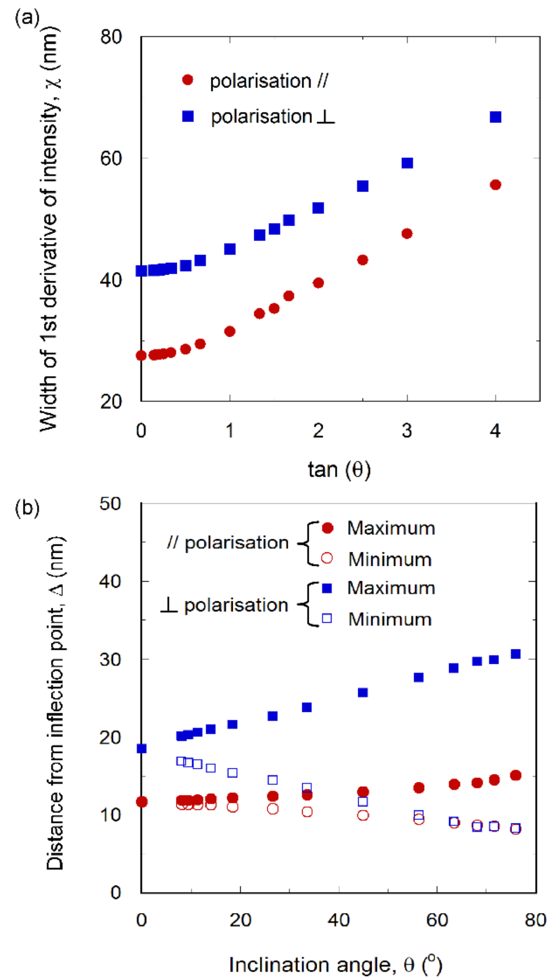

Figure 4 Imaging slanted heterojunctions. a Schematic of a sample with two regions of different PL or PC efficiency, the planar interface separating these regions being inclined at angle θ with respect to the surface. b Signal intensity, c its first derivative and d its second derivative plotted as the aperture crosses the interface, for inclination angels, θ, of 0°, 14°, 45° and 76°. The scan direction is parallel to the incident laser polarisation. For $\theta = 76°$, the inflection point of the signal intensity is marked as $\Omega_{76°}$ in b; the full-width at half-maximum (FWHM) of the first derivative is marked as $\Gamma_{76°}$ in c; and the separation between the inflection point and the minimum of the second derivative is marked as $\Delta_{76°}$ in d. Aperture radius, $a = 20\ nm$, tip-sample distance $z_0 = 5$ nm, sample refractive index $n = 1.62+0.54i$, laser wavelength $\lambda = 325\ nm$. The incident laser polarisation is perpendicular to the line where the interface meets the surface.